Polarimetric SAR Target Detection Using the Reflection Symmetry

Na Wang, Gongtao Shi, Li Liu, Lingjun Zhao, and Gangyao Kuang, *Member, IEEE*

***Abstract*—This letter addresses the polarimetric synthetic aperture radar target detection using the magnitude of the (2, 3) term in the sample averaged coherency matrix. The theoretical analysis demonstrates that such term reveals the difference between the nonreflection symmetric targets and natural clutters. The statistical models for such term are derived within different degrees of homogeneity. Based on the statistical models, an automatic constant-false-alarm-rate detection scheme is completed. The parameter estimation and the solution for the detection threshold are given in detail. Experimental results demonstrate the capability of the proposed approach for detecting ships, oil stores, buildings, etc., in homogeneous and heterogeneous areas.**

***Index Terms*—Constant false alarm rate (CFAR), detection, reflection symmetry.**

I. Introduction

THE problem of target detection using polarimetric synthetic aperture radar (POLSAR) data has received a great deal of attention in recent years. The studies on POLSAR target detection mainly utilize the polarimetric statistical and scattering information. Some of the excellent works include the polarimetric whitening filter detector [1], ship detection using polarization cross-entropy [2], and polarimetric target detector using the Huynen fork [3].

Except for the aforementioned algorithms, reflection symmetry is another important polarimetric scattering characteristic for detection. The reflection symmetry often holds true for natural clutters but rarely holds true for man-made targets [4]. The present studies mainly focus on polarimetric correlation coefficients. Some examples are power line detection using linear polarimetric correlation coefficients [5] and urban area extraction using circular polarimetric correlation coefficients [6]. The linear polarimetric correlation coefficients circumvent the difficulties of radiometric calibration [5]; however, the normalization of the mixed polarization term drops out the radiometric information of channels. The circular polarimetric correlation coefficient is effective in extracting urban structures in the vegetation area [6]; however, it is not efficient in detecting ships.

Manuscript received July 13, 2011; revised January 19, 2012 and February 14, 2012; accepted February 23, 2012.

The authors are with the College of Electronic Science and Engineering, National University of Defense Technology, Changsha 410073, China (e-mail: donggang.wang@gmail.com; shigongtao@sina.com; dreamliu2010@gmail.com; nudtzlj@163.com; Kuangyeats@vip.sina.com).

Color versions of one or more of the figures in this paper are available online at http://ieeexplore.ieee.org.

Digital Object Identifier 10.1109/LGRS.2012.2189548

In this letter, the magnitude of the (2, 3) term in the sample averaged coherency matrix is used for detection. The theoretical analysis demonstrates that such metric obviously reveals the reflection symmetry difference between most of the man-made targets and natural clutters. Moreover, it is easy for statistical modeling and favorable for implementing automatic detection using the constant-false-alarm-rate (CFAR) scheme. Of course, there are several typologies of targets such as horizontal and vertical wires or horizontal dihedrals, which are reflection symmetric. However, most of the man-made targets are composed of many strong scattering centers with different orientations, which make the whole structure of the targets not to be reflection symmetric. Therefore, the proposed detection method is applicable for many man-made targets such as ships, buildings, and oil stores.

II. Metric Used for Target Detection

Referring to the conclusions in [7], we present the differences between the nonreflection symmetric targets and reflection symmetric clutters from two aspects.

The first aspect is focused on the azimuth symmetry. When the elemental scatterer is oriented at 0° from the vertical polarization direction [8], the scattering matrix and the coherency matrix can be written as

$$S = \begin{bmatrix} S_{hh} & 0 \\ 0 & S_{vv} \end{bmatrix} \rightarrow T = \begin{bmatrix} T_{11} & T_{12} & 0 \\ T_{12}^* & T_{22} & 0 \\ 0 & 0 & 0 \end{bmatrix}. \tag{1}$$

Most of the mediums are composed of numerous scatterers with the orientation θ varying randomly. In such case, the coherency matrix of the scatterer can be written as

$$\tilde{T} = UTU^{\mathrm{T}} = \begin{bmatrix} T_{11} & T_{12}\cos 2\theta & -T_{12}\sin 2\theta \\ T_{12}^*\cos 2\theta & T_{22}\cos^2 2\theta & -0.5T_{22}\sin 4\theta \\ -T_{12}^*\sin 2\theta & -0.5T_{22}\sin 4\theta & T_{22}\sin^2 2\theta \end{bmatrix} \tag{2}$$

where the rotation matrix U is given in [7].

The azimuth slope may introduce orientation in the observed medium [7]. For most natural clutters such as ocean, vegetation, and forests, the orientation is generally assumed to be uniformly distributed. Assume that the orientation distribution of the scatterers is $p(\theta)$; then, $p(\theta)$ is considered to be centered at zero, and the averaged coherency matrix over $p(\theta)$ is derived as [7]

$$\overline{T} = \begin{bmatrix} T_{11} & \mu T_{12} & 0 \\ \mu T_{12}^* & \omega T_{22} & 0 \\ 0 & 0 & (1-\omega)T_{22} \end{bmatrix} \tag{3}$$

where $\mu = \int \cos 2\theta p(\theta) d\theta$ and $\omega = \int \cos^2 2\theta p(\theta) d\theta$.

Most man-made targets have regular shapes with deterministic orientation, which makes the orientation distribution of the scatterers not to be centered at zero. Assuming that the distribution $p(\theta)$ is centered at φ, the averaged coherency matrix is derived as (4) [7], shown at the bottom of the page.

The helix scattering term, which is used to reflect the co- and cross-polarized correlations in the four-component decomposition [4], may also be present in man-made targets since it can be generated by the combination of two or more coherent scatterers (e.g., diplanes [9]). For the right helix, the coherency matrix is

$$T_{\mathrm{rh}} = \frac{1}{2}\begin{bmatrix} 0 & 0 & 0 \\ 0 & 1 & j \\ 0 & -j & 1 \end{bmatrix}. \tag{5}$$

Due to the rotation invariance of (5), the averaged coherency matrix of the right helix $\overline{T}_{\mathrm{rh}}$ is equivalent to T_{rh}. This conclusion still holds for the left helix.

Comparing (3) with (4) and (5), it can be seen that the major differences between the reflection symmetric medium and nonreflection symmetric medium are the off-diagonal terms $\overline{T}_{13}$ and $\overline{T}_{23}$. For the reflection symmetric medium, both $\overline{T}_{13}$ and $\overline{T}_{23}$ are zero, as are shown in (3). For the nonreflection symmetric medium, $\overline{T}_{13}$ is $-T_{12}\mu \sin 2\varphi$, as is shown in (4), which is totally induced by the orientation of the scatterer. For the nonreflection symmetric medium, $\overline{T}_{23}$ is composed of two parts. The real part of $\overline{T}_{23}$ is $0.5T_{22}(1-2\omega)\sin 4\varphi$ [shown in (4)], which is also induced by the orientation of the scatterer. The imaginary part of $\overline{T}_{23}$, induced by the (2, 3) term of (5), corresponds to the helix scattering term. Compared with $\overline{T}_{13}$, it is obvious that $\overline{T}_{23}$ contains both the orientation and helicity information of the medium. Therefore, in this letter, the magnitude of $\overline{T}_{23}$ (denoted as $|\overline{T}_{23}|$) is used as a metric for detection.

III. Detection Algorithm

A. Statistical Modeling of $|\overline{T}_{23}|$

The 2×2 sample averaged coherency matrix containing the term $|\overline{T}_{23}|$ is written as

$$\overline{T} = \frac{1}{n}\sum_{i=1}^{n}\begin{bmatrix} |k_2(i)|^2 & k_2(i)k_3(i)^* \\ k_2(i)^*k_3(i) & |k_3(i)|^2 \end{bmatrix} = \begin{bmatrix} \overline{T}_{22} & |\overline{T}_{23}|e^{j\varphi} \\ |\overline{T}_{23}|e^{-j\varphi} & \overline{T}_{33} \end{bmatrix} \tag{6}$$

where n is the number of samples, k_1 and k_2 are the Pauli scattering vectors, i denotes the ith sample, φ is the phase of $\overline{T}_{23}$, and the superscript $*$ denotes the complex conjugate.

For a homogeneous area, the distribution of $|\overline{T}_{23}|$ is [10]

$$f\left(|\overline{T}_{23}|\right) = \frac{4n^{n+1}|\overline{T}_{23}|^n}{\Gamma(n)(1-\rho^2)h^{n+1}} I_0\left(\frac{2\rho n|\overline{T}_{23}|/h}{1-\rho^2}\right) \times K_{n-1}\left(\frac{2n|\overline{T}_{23}|/h}{1-\rho^2}\right) \tag{7}$$

where $I_0(\cdot)$ and $K_{n-1}(\cdot)$ are the first- and second-kind modified Bessel functions with orders 0 and $n-1$, respectively. ρ is the correlation coefficient between k_2 and k_3, which is defined by

$$\rho = \left|\frac{E\left[k_2(i)k_3(i)^*\right]}{\sqrt{E\left[|k_2(i)|^2\right]}\cdot\sqrt{E\left[|k_3(i)|^2\right]}}\right| = \frac{|R_{12}|}{\sqrt{R_{11}}\cdot\sqrt{R_{22}}} = \frac{|R_{12}|}{h} \tag{8}$$

where R_{ij} ($i = 1, 2$ and $j = 1, 2$) is the statistical average of $\overline{T}_{ij}$.

It is difficult to estimate the parameters and calculate the detection threshold of (7) because of the product of Bessel functions. A possible way to circumvent this problem is to approximate the product of $I_0(\cdot)$ and $K_{n-1}(\cdot)$ with a simpler expression. For the large argument, the asymptotic expansions of $I_0(\cdot)$ and $K_{n-1}(\cdot)$ are given in [11]; then, the product of $I_0(\cdot)$ and $K_{n-1}(\cdot)$ in (7) can be approximated by

$$P\left(|\overline{T}_{23}|, h, n, \rho\right) \approx V\left(|\overline{T}_{23}|, h, n, \rho\right) \cdot \sum_{k=0}^{K}\sum_{m=0}^{K}\left[\frac{(-1)^k\Gamma\left(k+\frac{1}{2}\right)\Gamma\left(n+m-\frac{1}{2}\right)\left(\frac{(1-\rho^2)}{4n|\overline{T}_{23}|/h}\right)^{k+m}}{\Gamma\left(\frac{1}{2}-k\right)\Gamma(k+1)\Gamma(m+1)\Gamma\left(n-\frac{1}{2}-m\right)\rho^{k+1/2}}\right] \tag{9}$$

where

$$V\left(|\overline{T}_{23}|, h, n, \rho\right) = \frac{(1-\rho^2)}{4n\sqrt{\rho}|\overline{T}_{23}|/h}\exp\left(-\frac{2n|\overline{T}_{23}|/h}{(1+\rho)}\right). \tag{10}$$

For natural clutters, the parameter ρ is small, which makes the arguments in $I_0(\cdot)$ and $K_{n-1}(\cdot)$ also to be small. In such case, the approximation error caused by the asymptotic expansions of $I_0(\cdot)$ and $K_{n-1}(\cdot)$ cannot be neglected; thus, $P(|\overline{T}_{23}|, h, n, \rho)$ in (9) cannot be approximated by the product of $V(|\overline{T}_{23}|, h, n, \rho)$ and the double sum. Instead, we check if the quotient of $P(|\overline{T}_{23}|, h, n, \rho)$ divided by $V(|\overline{T}_{23}|, h, n, \rho)$ [denoted as $U(|\overline{T}_{23}|, h, n, \rho)$] can be approximated by a constant. In the following, $P(|\overline{T}_{23}|, h, n, \rho)$, $V(|\overline{T}_{23}|, h, n, \rho)$, and $U(|\overline{T}_{23}|, h, n, \rho)$ are denoted as P, V, and U for convenience.

We select two patches from the two data sets, which are used for detection in this letter, and calculate the values of P, V, and U numerically. Patch 1 is the sea area, shown in the red rectangle in Fig. 3(a). Patch 2 is the vegetation area, shown in the red rectangle in Fig. 3(b). It is too compressed to presenting the value of all the samples of the patches. For a better visualization, we only select an interval including 800 samples and plot the corresponding values of P, V, and U,

$$\overline{T} = \begin{bmatrix} T_{11} & T_{12}\mu\cos 2\varphi & -T_{12}\mu\sin 2\varphi \\ T_{12}^*\mu\cos 2\varphi & T_{22}(\sin^2 2\varphi + \omega\cos 4\varphi) & 0.5T_{22}(1-2\omega)\sin 4\varphi \\ -T_{12}^*\mu\sin 2\varphi & 0.5T_{22}(1-2\omega)\sin 4\varphi & T_{22}(\cos^2 2\varphi - \omega\cos 4\varphi) \end{bmatrix} \tag{4}$$

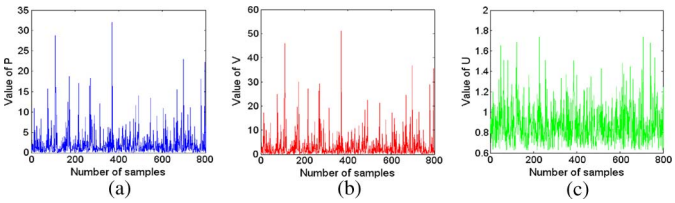

Fig. 1. Numerical calculation results of 800 samples from patch 1. (a) $P(|\overline{T}_{23}|, h, n, \rho)$. (b) $V(|\overline{T}_{23}|, h, n, \rho)$. (c) $U(|\overline{T}_{23}|, h, n, \rho)$.

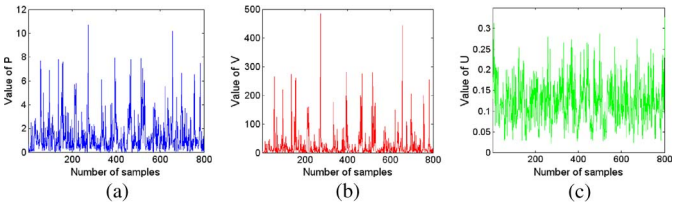

Fig. 2. Numerical calculation results of 800 samples from patch 2. (a) $P(|\overline{T}_{23}|, h, n, \rho)$. (b) $V(|\overline{T}_{23}|, h, n, \rho)$. (c) $U(|\overline{T}_{23}|, h, n, \rho)$.

shown in Figs. 1 and 2. In both figures, it can be seen that the variation of the P value is similar to that of U. Thus, except that a very few points have larger U value, the value of most pixels varies in a small scope. For the few points with large U value, the corresponding $|\overline{T}_{23}|$ value is much larger. It leads to the values of P and V of approximately zero, so the numerical calculated value of U is singular. Such kind of singular points causes large fluctuation in the interval; however, they are very few in the homogeneous area and thus have little effect on the statistical distribution of samples.

When U is considered as a constant (denoted as m_0), according to (9) and (10), (7) can be simplified as

$$f\left(|\overline{T}_{23}|\right) = \frac{4n^{n+1}|\overline{T}_{23}|^n}{\Gamma(n)(1-\rho^2)h^{n+1}} \cdot V\left(|\overline{T}_{23}|, h, n, \rho\right) \cdot m_0 = \frac{n^n\left(|\overline{T}_{23}|/h\right)^{n-1} m_0}{h\Gamma(n)\sqrt{\rho}} \exp\left(-\frac{2n|\overline{T}_{23}|/h}{(1+\rho)}\right). \quad (11)$$

According to $\int_0^\infty f(|\overline{T}_{23}|)d|\overline{T}_{23}| = 1$, we get $m_0 = 2^n/(1+\rho)^n$; then, (11) is written as

$$f\left(|\overline{T}_{23}|\right) = \frac{a_0 n^n}{h\Gamma(n)}\left(a_0|\overline{T}_{23}|/h\right)^{n-1} \times \exp\left(-\frac{na_0|\overline{T}_{23}|}{h}\right) a_0, \qquad n > 0 \quad (12)$$

where $a_0 = 2/(1+\rho)$. It can be seen that (12) is the Gamma distribution. It should be clarified that the Gamma distribution is just a particular case of (7). However, compared with (7), the Gamma distribution is more tractable in the parameter estimation and detection. Moreover, based on the Gamma distribution, the statistical distribution of the heterogeneous area can be easily derived and is also easy to implement in CFAR detection, as is presented in Section III-B and C.

To further validate the feasibility of the Gamma distribution in the statistical modeling of $|\overline{T}_{23}|$, the fitting results of (12) for the two patches are shown in Fig. 4(a) and (b). In Fig. 4(a), the Gamma distribution (marked as the blue solid line) is fitted well with the histogram (marked as the black dots) in patch 1. Even in patch 2, the fitting result is also acceptable. The corresponding values of the Kullback–Leibler (KL) distance

TABLE I
VALUES OF THE KL DISTANCE, KS TEST, AND MSE IN THE TWO PATCHES

Labeled	KL			KS			MSE		
Patches	Gamma	K	G^0	Gamma	K	G^0	Gamma	K	G^0
Patch 1	0.006	0.0012	0.001	0.0066	0.0053	0.0039	0.0006	0.0005	0.0005
Patch 2	0.0036	0.0141	0.0029	0.0127	0.0101	0.0119	0.0016	0.0014	0.0014

[12], Kolmogorov–Smirnov (KS) test [12], and mean-square error (mse) [12] (listed in Table I) are also small. According to the aforementioned results, it can be seen that the variation of U in a small scope has minor effect in the statistical modeling of clutter. Therefore, the Gamma distribution seems to be reasonable in modeling $|\overline{T}_{23}|$ in the homogeneous area.

For heterogeneous regions, the radar cross section (RCS) is often modeled by the Gamma distribution. Then, grounded on the product model, $|\overline{T}_{23}|$ follows the K distribution [13]. For highly heterogeneous regions, the RCS is often modeled by the reciprocal of Gamma distribution [13]. In such case, $|\overline{T}_{23}|$ follows the G^0 distribution. It is also a kind of Fisher distribution [12] and is written as

$$f\left(|\overline{T}_{23}|\right) = \frac{a_0 n^n \Gamma(n-\alpha)}{h\lambda^\alpha \Gamma(n)\Gamma(-\alpha)} \frac{\left(a_0|\overline{T}_{23}|/h\right)^{n-1}}{\left(\lambda + na_0|\overline{T}_{23}|/h\right)^{n-\alpha}} \quad (13)$$

where $a_0 = 2/(1+\rho)$ and n, α, and λ are the effective number of looks, the shape parameter, and the scale parameter, respectively.

Both the K and G^0 distributions have more extensive modeling capacity than the Gamma distribution. However, compared with the K distribution, the G^0 distribution does not contain the Bessel function; thus, it is easier for parameter estimation and calculating the accumulated distribution function [13]. Therefore, we only use the G^0 distribution for CFAR detection. The parameter estimation and the solution for the detection threshold of the G^0 distribution are presented in Sections III-B and C.

B. Parameter Estimation for the G^0 Distribution

For a homogeneous area, the parameter ρ is often estimated using the following formula [5]:

$$\hat{\rho} = \frac{\left|\sum_{k=1}^N k_2(k)k_3(k)^*\right|}{\sqrt{\sum_{k=1}^N |k_2(k)|^2 \sum_{k=1}^N |k_3(k)|^2}} = \frac{\overline{T}_{12}}{\sqrt{\overline{T}_{11}}\cdot\sqrt{\overline{T}_{22}}} \quad (14)$$

where N is the number of samples. Equation (14) has been proved to be asymptotic unbiased [5]. It is still valid for a heterogeneous area since the statistical average of the RCS can be factored and canceled out of the numerator and denominator.

The parameter h is estimated in the homogeneous area. According to the multivariate statistical analysis theory, the principal diagonal elements $\overline{T}_{11}$ and $\overline{T}_{22}$ in (6) are the unbiased estimation of the elements R_{11} and R_{22} in (8), respectively. Then, the parameter h is estimated by

$$\hat{h} = \sqrt{\hat{R}_{11}}\cdot\sqrt{\hat{R}_{22}} = \sqrt{\overline{T}_{11}}\cdot\sqrt{\overline{T}_{22}}. \quad (15)$$

The other parameters of the G^0 distribution are estimated using the "second-kind statistics" method [12]. Such method

yields a very simple parameter estimation expression for the G^0 distribution, as is derived as

$$\begin{cases} \hat{\tilde{c}}_1 = \ln(\hat{\lambda}\hat{h}/(\hat{a}_0\hat{n}) + \Psi(\hat{n}) - \Psi(-\hat{\alpha}) = \frac{1}{N}\sum_{i=1}^{N}[\ln(x_i)] \\ \hat{\tilde{c}}_k = \Psi(k,\hat{n}) + (-1)^k\Psi(k,-\hat{\alpha}) = \frac{1}{N}\sum_{i=1}^{N}\left[(\ln(x_k) - \hat{\tilde{c}}_1)^k\right] \end{cases} \tag{16}$$

where x_i is the ith sample. $\tilde{c}_k$ is the kth logarithmic cumulant of the sample; $\Psi(k)$ $(k = 1, 2, \ldots)$ denotes the digamma function. $\Psi(k, \cdot)$ denotes the polygamma function of kth order. $-\hat{\alpha}$, $\hat{\lambda}$, and $\hat{n}$ are the estimated parameters.

C. Solution for the CFAR Detection Threshold

For the G^0 distribution, the CFAR detection threshold T is obtained by solving the following equation:

$$1 - f_a = \frac{\Gamma(n-\alpha)}{\Gamma(n)\Gamma(-\alpha)}\left(\frac{a_0 n}{\lambda h}\right)^n \times \int_0^T \frac{|\overline{T}_{23}|^{n-1}}{\left(1 + a_0 n|\overline{T}_{23}|/\lambda h\right)^{n-\alpha}} d|\overline{T}_{23}| \tag{17}$$

where f_a is the false alarm rate. According to the integral equation in [14]

$$\int_0^u x^{\mu-1}/(1+\beta x)^v dx = (u^\mu/\mu)\,{}_2F_1(v, \mu; 1+\mu; -\beta u) \tag{18}$$

(17) is derived as

$$(\lambda h)^n\Gamma(n)\Gamma(-\alpha)(1-f_a) - a_0^n n^{n-1}\Gamma(n-\alpha) \cdot {}_2F_1\left(n-\alpha, n; n+1; -(a_0 n/\lambda h)T\right)T^n = 0 \tag{19}$$

where ${}_2F_1(a, b; c; d)$ is the Gauss hypergeometric function. The threshold T in (19) is solved numerically.

IV. Experimental Result

The proposed detection method is evaluated using two POLSAR data sets acquired by RADARSAT-2, with a resolution of 12 m × 12 m in the range and azimuth. Data set 1 is the sea area of San Francisco, CA. The image size is 850 × 408 pixels. The Pauli color composite image is shown in Fig. 3(a) with HH + VV (blue), HH − VV (red), and 2HV (green), where the ship targets are indicated by the blue ellipses. Data set 2 was acquired in Vancouver, BC, Canada. The image size is 415 × 388 pixels. The Pauli color composite image is shown in Fig. 3(b), where the targets are mainly the buildings indicated by the blue ellipses and the oil stores indicated by the yellow ellipses, and the clutter is mainly the vegetation area composed of trees. The optical image of data set 2 is also presented as an approximation to the ground truth, as is shown in Fig. 3(c). Before data analysis, the spatial average is applied to the data using a 7 × 7 window over the pixels.

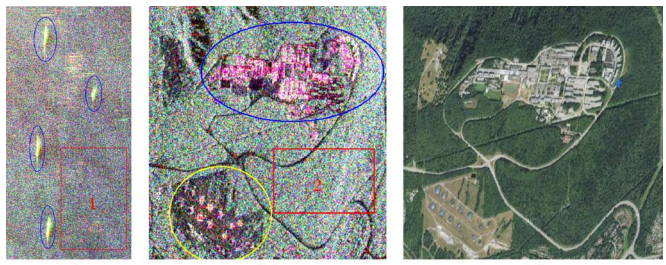

Fig. 3. (a) Pauli color composite image of data set 1. (b) Pauli RGB image of data set 2. (c) Optical image of data set 2 (Google Earth).

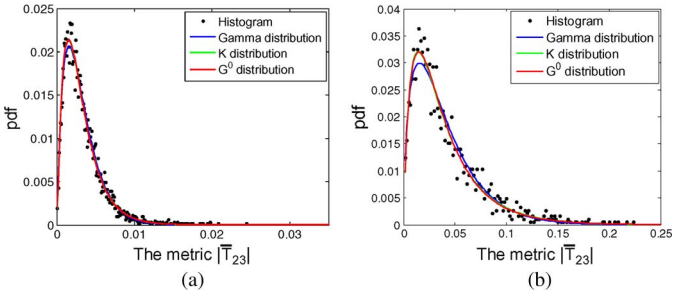

Fig. 4. Fitting results of the three distributions for the two labeled patches. (a) Results in patch 1. (b) Results in patch 2.

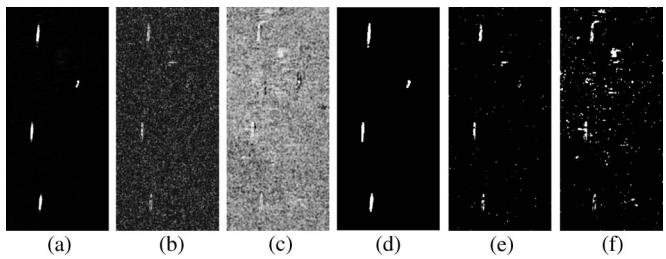

Fig. 5. (a) $|\overline{T}_{23}|$. (b) $|\rho_{HHHV}|$. (c) $|\rho_{RRLL}|$. (d) Detection result of $|\overline{T}_{23}|$. (e) Detection result of $|\rho_{HHHV}|$. (f) Detection result of $|\rho_{RRLL}|$.

A. Goodness of Fit Results

Fig. 4 shows the fitting results of the Gamma, K, and G^0 distributions for the histograms of $|\overline{T}_{23}|$ in the two labeled patches, which have been described in Section III-A. It can be seen that the results of the Gamma distribution are worse than those of the K and G^0 distributions in the two patches, particularly in patch 2. The fitting results of the K and G^0 distributions are comparable in both patches. The KL distance, KS test, and mse values in Table I also validate the aforementioned conclusion. However, the K distribution contains the Bessel function; thus, it is more difficult to be applied in CFAR detection.

B. Detection Results and Analysis

Fig. 5(a) shows the metric $|\overline{T}_{23}|$ of data set 1. It can be observed that the contrast between the ships and sea is very distinct, i.e., the pixels of the ships are much brighter and the pixels of the sea are much darker. The absolute value of the linear polarimetric correlation coefficient between HH and HV channels (denoted as $|\rho_{HHHV}|$) is shown in Fig. 5(b). It can be seen that the $|\rho_{HHHV}|$ value between the ships and sea is not so distinct as $|\overline{T}_{23}|$. The absolute value of the circular

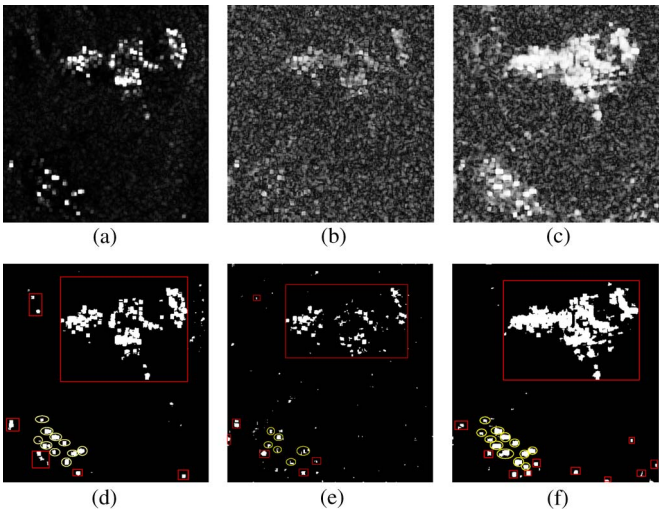

Fig. 6. (a) $|\overline{T}_{23}|$. (b) $|\rho_{HHHV}|$. (c) $|\rho_{RRLL}|$. (d) Detection result of $|\overline{T}_{23}|$. (e) Detection result of $|\rho_{HHHV}|$. (f) Detection result of $|\rho_{RRLL}|$.

polarimetric correlation coefficient in [6] (denoted as $|\rho_{RRLL}|$) is shown in Fig. 5(c). It can be seen that the $|\rho_{RRLL}|$ value between the ships and sea does not present large differences. The reason is that the sea is dominated by the surface scattering and the ships are dominated by the double-bounce scattering. The double-bounce scattering and the surface scattering all have large $|\rho_{RRLL}|$ value [6].

The CFAR detection result of $|\overline{T}_{23}|$ is shown in Fig. 5(d) with the false alarm rate $f_a = 0.001$. It can be seen that the regions of interest (ROIs) of the ships are all detected; moreover, there are almost no false alarms in the analyzed area. $|\rho_{HHHV}|$ and $|\rho_{RRLL}|$ are detected by selecting the appropriate threshold, shown in Fig. 5(e) and (f). In Fig. 5(e), the ROIs of the ships are not so completed as those in Fig. 5(d); moreover, there exist many false alarms. The result in Fig. 5(f) is much worse than those in Fig. 5(d) and (e) due to the minor difference between the $|\rho_{RRLL}|$ values of the ship and sea pixels.

Fig. 6(a)–(c) shows $|\overline{T}_{23}|$, $|\rho_{HHHV}|$, and $|\rho_{RRLL}|$ of data set 2. In Fig. 6(a), it can be seen that the buildings and oil stores are brighter than the vegetation area. In Fig. 6(b), the $|\rho_{HHHV}|$ value between the targets and vegetation area does not present large differences. In Fig. 6(c), the buildings and oil stores are much brighter than the vegetation area. It is because the buildings and oil stores are dominated by the even- and odd-bounce scattering and the vegetation area is dominated by the volume scattering. The $|\rho_{RRLL}|$ value of the volume scattering is much less than that of the even- and odd-bounce scattering [6].

The CFAR detection result of $|\overline{T}_{23}|$ is shown in Fig. 6(d) with $f_a = 10^{-3}$, and the detection results of $|\rho_{HHHV}|$ and $|\rho_{RRLL}|$ are shown in Fig. 6(e) and (f), respectively. By visual inspection, most of the detected buildings in the three figures are marked by the red rectangles, and most of the detected oil stores are marked by the yellow ellipses. Among the three figures, it can be seen that the detection result of $|\rho_{HHHV}|$ is worst, represented by the most false alarms and least detected targets, and the result of $|\overline{T}_{23}|$ is a little worse than that of $|\rho_{RRLL}|$. The false alarms in Fig. 6(d) are mainly caused by slopes in the vegetation area, which make the reflection symmetry to no longer hold.

V. Conclusion

In this letter, the magnitude of the (2, 3) term in the sample averaged coherency matrix has been used to detect the nonreflection symmetric targets. After visual inspection of the detection masks, it can be concluded that such term is better than the linear and circular polarimetric correlation coefficients to discriminate between the ships and sea and is a little worse than the circular polarimetric correlation coefficient in detecting the urban structures. However, it is easy for realizing the automatic detection by implementing the CFAR scheme; thus, it is applicable for detecting the nonreflection symmetric targets. It should be pointed out that the detection results are just a visual inspection. Further validations with ground truth will be carried out in the future. Moreover, in order to improve the robustness of the proposed method, the detection in the land area needs to be developed more in the future.

Acknowledgment

The authors would like to thank the anonymous reviewers for their constructive advice and pertinent comments.

References

[1] L. M. Novak and M. C. Burl, "Studies of target detection algorithms that use polarimetric radar data," *IEEE Trans. Aerosp. Electron. Syst.*, vol. 25, no. 2, pp. 150–165, Mar. 1989.

[2] J. Chen, Y. Chen, and J. Yang, "Ship detection using polarization cross-entropy," *IEEE Geosci. Remote Sens. Lett.*, vol. 6, no. 4, pp. 723–727, Oct. 2009.

[3] A. Marino, S. R. Cloude, and H. Iain, "A polarimetric target detector using the Huynen fork," *IEEE Trans. Geosci. Remote Sens.*, vol. 48, no. 5, pp. 2357–2366, May 2010.

[4] Y. Yamaguchi, Y. Yajima, and H. Yamada, "A four-component decomposition of POLSAR images based on the coherency matrix," *IEEE Geosci. Remote Sens. Lett.*, vol. 3, no. 3, pp. 292–296, Jul. 2006.

[5] K. Sarabandi and M. Park, "A statistical theory of power line detection in polarimetric MMW SAR images," in *Proc. IEEE Antennas Propag. Soc. Int. Symp.*, Jul. 2000, vol. 4, pp. 2150–2153.

[6] T. Moriyama, S. Uratsuka, T. Umehara, M. Satake, and Y. Yamaguchi, "A study on extraction of urban areas from polarimetric synthetic aperture radar image," in *Proc. IEEE IGARSS*, Sep. 2004, pp. 703–706.

[7] J.-S. Lee, D. L. Schuler, T. L. Ainsworth, E. Krogager, D. Kasilingam, and W.-M. Boerner, "On the estimation of radar polarization orientation shifts induced by terrain slopes," *IEEE Trans. Geosci. Remote Sens.*, vol. 40, no. 1, pp. 30–41, Jan. 2002.

[8] A. Freeman and S. L. Durden, "A three-component scattering model for polarimetric SAR data," *IEEE Trans. Geosci. Remote Sens.*, vol. 36, no. 3, pp. 963–973, May 1998.

[9] E. Krogager, "Aspects of polarimetric radar imaging," Ph.D. dissertation, Tech. Univ. Denmark, Copenhagen, Denmark, May, 1993.

[10] J.-S. Lee, K. W. Hoppel, S. A. Mango, and A. R. Miller, "Intensity and phase statistics of multilook polarimetric and interferometric SAR imagery," *IEEE Trans. Geosci. Remote Sens.*, vol. 32, no. 5, pp. 1017–1028, Sep. 1994.

[11] C. H. Gierull, "Statistical analysis of multilook SAR interferograms for CFAR detection of ground moving targets," *IEEE Trans. Geosci. Remote Sens.*, vol. 42, no. 4, pp. 691–701, Apr. 2004.

[12] C. Tison, J.-M. Nicolas, F. Tupin, and H. Maître, "A new statistical model for Markovian classification of urban areas in high-resolution SAR images," *IEEE Trans. Geosci. Remote Sens.*, vol. 42, no. 10, pp. 2046–2057, Oct. 2004.

[13] M. Mejail, A. C. Frery, J. Jacobo-Berlles, and F. Kornblit, "Approximation of the KA distribution by the GA0 distribution," in *Proc. Anais IX Simposio Brasileiro Sensoriamento Remoto*, Santos, Brazil, Sep. 1998, pp. 1121–1132.

[14] I. S. Gradshteyn and I. M. Ryzhik, *Table of Integrals, Series, and Products*, 7th ed. San Diego, CA: Academic, 2007.